www.nature.com/scientificreports

scientific reports

Check for updates

OPEN

Physical analysis of high refractive index metamaterial-based radiation aggregation engineering of planar dipole antenna for gain enhancement of mm-wave applications

Mohammad Lutful Hakim[1,2], Mohammad Tariqul Islam[2]✉, Touhidul Alam[1], Abdulmajeed M. Alenezi[3], Mandeep Singh Jit Singh[2], Md. Shabiul Islam[4]✉ & Mohamed S. Soliman[5]

A metamaterial-incorporated high-gain and broadband dipole antenna is proposed for 5G mm-wave applications. The designed high refractive index metamaterial (HRIM) properties are presented in detail with supporting results. The proposed dipole antenna achieved broadband features, and the antenna gain increased significantly by incorporating HRIM in the electromagnetic (EM) wave propagation path. Besides, the EM wave aggregation engineering of utilizing the HRIM on the dipole antenna is analyzed using the electric field, magnetic field, and power flow distributions. Both conventional and HRIM-based dipole antenna (HRIMDA) were fabricated on thin (0.254 mm) Rogers RT5880 substrate material with a low dielectric constant of 2.2, where the noticeable gain enhancement by HRIM is observed. The measured results show the operational bandwidth (BW) from 23 to 38 GHz frequency, and the highest gain of 9.5 dBi is accomplished at 35 GHz frequency. Finally, a four-element MIMO configuration is numerically and experimentally analyzed where the isolation of the two conjugated MIMO elements is < – 20 dB. The MIMO parameters like envelop correlation coefficient (ECC) < 1×10^{-3} and diversity gain (DG) value of > 9.9 were also achieved. Hence, the proposed HRIM base dipole antenna is a potential candidate for 5G mm-wave applications.

Keywords Metamaterial, Mm-Wave, Broadband, Gain enhancement, Wireless communications

The upcoming wireless communications system is the mm-wave fifth-generation (5G) technology. Because of the exponentially growing demands of high data rates with low latency and inadequate BW in the microwave frequency (sub-6 GHz), the upcoming advanced communication system will be implemented in mm-wave frequency region mainly from 24 to 100 GHz[1]. The 5G mm-wave communications are expected to revolutionize daily life through its excellent connectivity with modern technology like smart factories, automotive cars, smart homes, telemedicine, virtual reality, etc.[2–5]. Standardization organizations, telecom companies, and government authorities are working on deploying and standardizing mm-wave 5G communications systems. The 26 GHz, 28 GHz, 37 GHz, and 38 GHz frequencies are allocated by different countries for 5G new radio (NR)[6,7]. As a

[1]Pusat Sains Angkasa (ANGKASA), Institut Perubahan Iklim, Universiti Kebangsaan Malaysia, UKM, 43600 Bangi, Selangor, Malaysia. [2]Department of Electrical, Electronic and Systems Engineering, Faculty of Engineering and Built Environment, Universiti Kebangsaan Malaysia, 43600 Bangi, Malaysia. [3]Department of Electrical Engineering, Faculty of Engineering, Islamic University of Madinah, 41411 Madinah, Saudi Arabia. [4]Faculty of Engineering (FOE), Multimedia University, Persiaran Multimedia, 63100 Cyberjaya, Selangor, Malaysia. [5]Department of Electrical Engineering, College of Engineering, Taif University, P.O. Box 11099, 21944 Taif, Saudi Arabia. ✉email: tariqul@ukm.edu.my; shabiul.islam@mmu.edu.my

result, antenna development in mm-wave frequency has gained significant importance in recent years[8]. Patch antennas are attractive for their low profile, low cost, and planar structure, but they have disadvantages such as low gain and narrow bandwidth[9–11]. The planar antenna with high gain in communication systems is attractive for satellite or base station applications. The upcoming 5G wireless communication systems will be implemented in the mm-wave frequency, but these frequencies go through high free space path loss. Hence, the communication range degrades than the 4G (fourth generation) frequency band. High-gain antennas are required on both ends of the communication device to overcome atmospheric and high propagation loss in mm-wave frequency[12,13]. From this perspective, the metamaterial is a strong candidate for designing an antenna with this required feature[14–18]. Various works were done to increase the antenna performance, such as gain and bandwidth. Usually, the metamaterial is positioned on the antenna radiating element or behind the defected ground antenna[19], where the gap between the antenna and meta-surface layer increases the bulkiness and complexity of the antenna. An antenna coupled with a metamaterial superstrate, where a lens is positioned on the radiating patch, can enhance the gain by focusing the radiation beam. This type of antenna can provide wideband operational frequency but suffers from low radiation efficiency because of its bulky size and losses in the thick dielectric material. In research[20–22], the antenna gain significantly increases by arranging the metamaterial superstrate on the antenna patch, but this technique has mechanical complexity and high-profile properties because of the air cavity among the superstrate and antenna. Similarly, a metamaterial structure is vertically placed to increase the gain of the bow-tie antenna[23]. In[24,25], metamaterial was vertically positioned in the direction of the EM wave propagation to enhance the gain. The meta-surface without any air gap can improve the performance of the planar antenna by utilizing the multiple layers technique, but this can increase the design complexity of the antenna. Also, this arrangement has some major disadvantages, such as bulkiness, narrowband, and increased fabrication cost. Alternately, the antenna array configurations can achieve a high gain, but they provide a similar channel capacity to a single antenna because the array antenna is fed by a single port like a single antenna and also suffers from power loss in complex power divider networks[26]. On the other hand, meta-surface was generally used with patch and slot antennas because of their controlling property of EM waves[6]. Single-layer antennas with metamaterial were presented in[20–23], where most are in the microwave range and have low gain or bandwidth. However, the MIMO performance of these antennas was not investigated. The MIMO performance analysis is crucial for this mm-wave frequency range because the MIMO antenna will provide multiple channels for increasing the data traffic, spectral efficiency, link reliability and capacity[27–29]. Hence, the antenna with a MIMO configuration is the key requirement for mm-wave 5G applications[30]. After the above discussions, a high-gain antenna with a larger operational bandwidth is highly recommended for mm-wave 5G applications; moreover, MIMO performance analysis is also essential.

This paper presents a metamaterial incorporated planar dipole antenna for mm-wave 5G applications. The designed HRIMDA gain is increased by 3.5 dBi, using five series of horizontal H-shape metamaterial structures and operational bandwidth from 23 to 38 GHz. The investigation of the MIMO configurations of HRIMDA shows the high isolation among two conjugated antennas, which is < – 30 dB. The MIMO parameters like ECC and DG values are < 0.0001 and > 9.99, respectively, which are the near-ideal values. Finally, the proposed HRIMDA has a high gain and a more comprehensive operational bandwidth at mm-wave frequency. Moreover, the MIMO configuration shows excellent parametric behaviour, which makes the planned antenna attractive for mm-wave 5G applications.

Metamaterial unit cell design

Metamaterials (MTMs) are commonly referred to as artificial materials with unique, effective medium characteristics that are not generally found in nature. These unique properties, like negative permittivity and permeability, gained significant attention in various applications like antenna design, clocking, and sensing[31–33]. The electric and magnetic quantities, also known as essential parameters, explain a medium's EM wave behaviour. This article presents a horizontal H-shaped metamaterial resonator for gain enhancement over the more extensive mm-wave frequency range. The proposed horizontal H shape metamaterial is designed on the Rogers RT5880 substrate material with a thin 0.254 mm thickness. The parametric sketch is presented in Fig. 1a, where a = 1.6 nm, r = 1.10 nm, w = 0.10 nm, and g = 0.50 nm, respectively. The simulation setup of the designed MTM is presented in Fig. 1b, where a perfect electric conductor (PEC) and perfect magnetic conductor (PMC) are applied along the y and z axes, respectively. The EM wave is applied along the x-axis in a positive direction. The simulation of the proposed MTM is done by the CST microwave studio[34].

The MTM electromagnetic property can be characterized by the Lorentz-Drude model. The Eqs. (1–3) are used to calculate the relative permittivity (ε_r), relative permeability (μ_r) and effective refractive index (η_r),[35,36]. Where, S_{11} and S_{21} are the reflection and transmission coefficients, respectively. d is the propagation distance of the medium, and K_o is the wave number.

$$\varepsilon_r = {}^{2}\!/_{jk_0 d} \times {}^{(1 - S_{11} - S_{21})}\!/_{(1 + S_{11} + S_{21})} \tag{1}$$

$$\mu_r = {}^{2}\!/_{jk_0 d} \times {}^{(1 - S_{21} + S_{11})}\!/_{(1 + S_{21} - S_{11})} \tag{2}$$

$$\eta = \sqrt{\varepsilon_r \mu_r} \tag{3}$$

Figure 2 demonstrates the EM parameters property of the intended horizontal-H shape MUC, which shows permittivity near zero (ENZ) value at the upper-frequency region. The permeability near zero (MNZ) has appeared from the lower operating frequencies to 35 GHz. This permittivity and permeability value leads to a

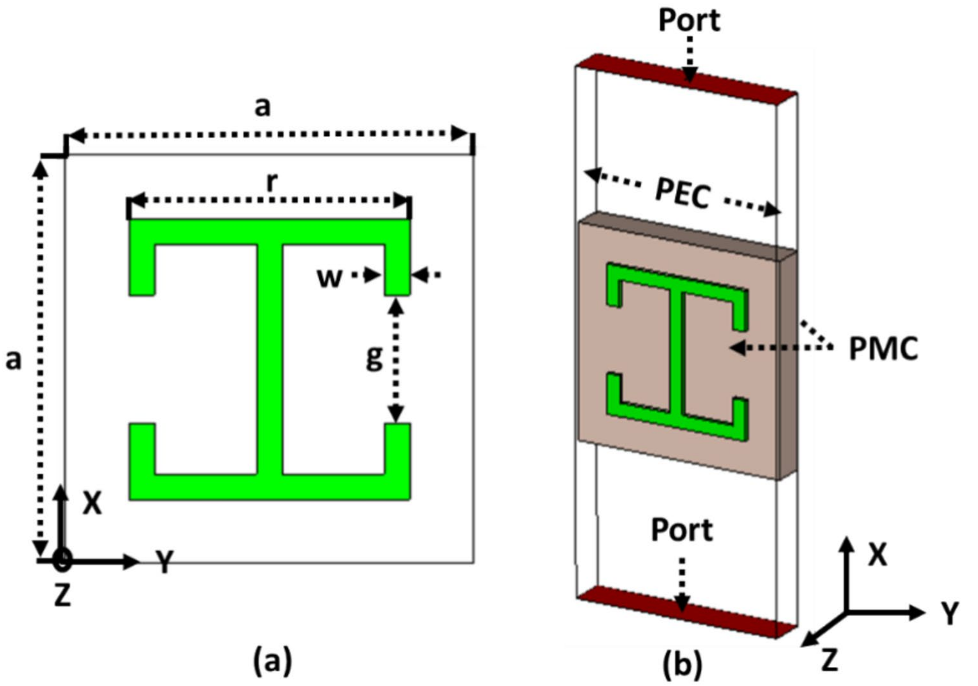

Fig. 1. Horizontal H shape metamaterial unit cell (MUC) (**a**) front view and (**b**) simulation setup.

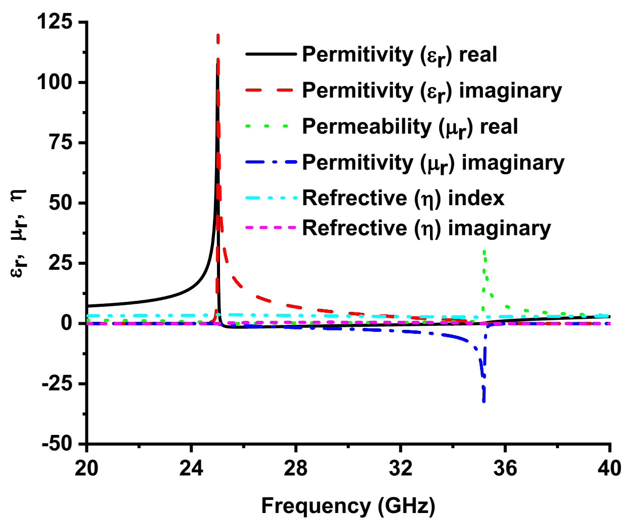

Fig. 2. Metamaterial property of the designed horizontal H shape MUC.

higher index metamaterial. The real value of the refractive index shows a higher refractive index metamaterial (HRIM) property than the air medium. This metamaterial property is used to enhance the antenna's performance in terms of gain and directivity[37] and provides a unique way to control the direction of the EM radiation based on Snell's law. Figure 3 presents the EM wave propagation from air to HRIM and HRIM to air. According to Snell's law, when an incident angle θ_i fixed the refracted angle θ_r shows a smaller value for EM wave propagation through a low-index to high-index medium. On the other hand, for the same conditions, the EM wave shows a larger refracted angle when propagating through the high index to the low-index medium. Based on this, a metamaterial lens can be formed and can be focused on the EM wave in the direction of propagation and aggregate the beam towards the end-fire direction[38]. The energy transmitted through metamaterial congregates and is intense in the direction of propagation. This type of MTM can enhance the gain and directivity of the antenna. The EM wave aggregation property can be understood from the metamaterial's electric (E) field[39], where a spherical wave converts to a planar wave and decreases the half-power beamwidth by metamaterial. This process was implemented by various metamaterial structures on planar antenna[39,40].

The characteristics of the metamaterial are analyzed by surface current allocation, E-field, and H-field distribution, shown in Fig. 4. The relationship between these three field distributions can be understood by analyzing

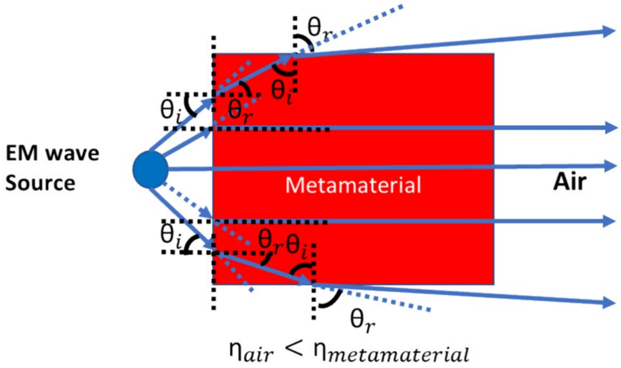

Fig. 3. EM wave propagation through designed HRIM.

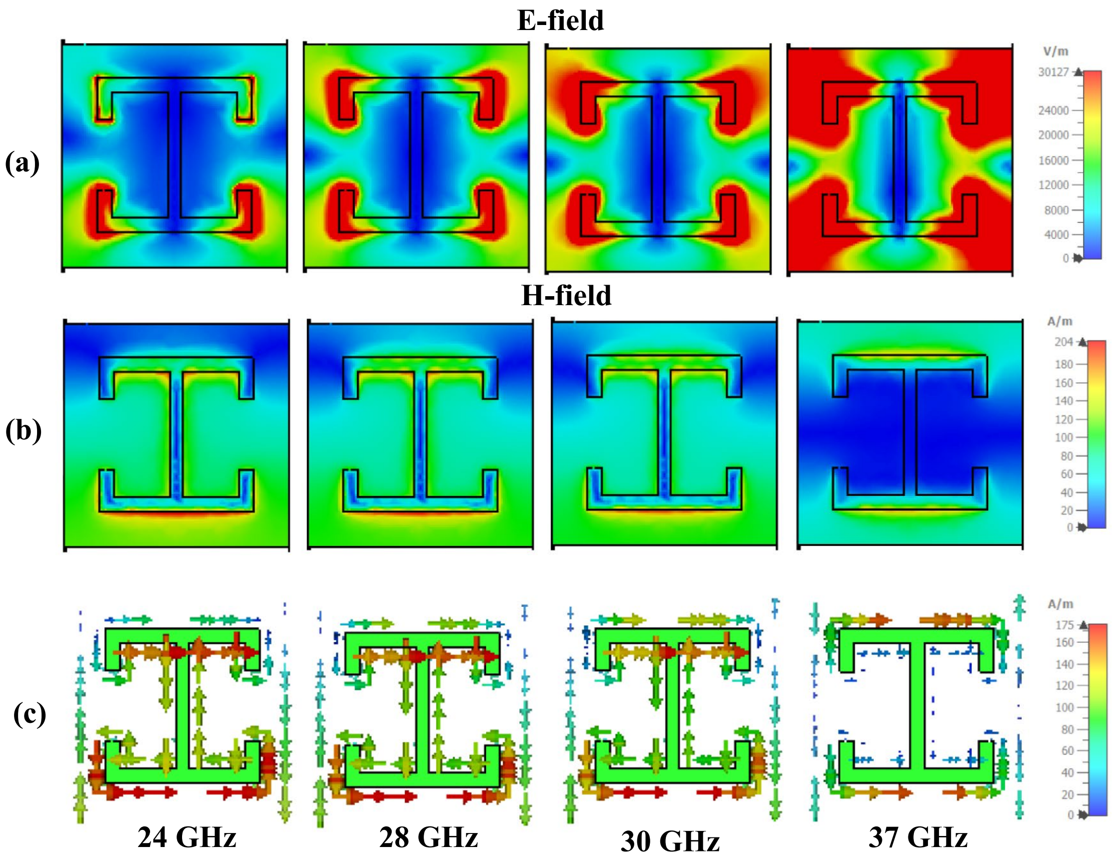

Fig. 4. (**a**) E-field. (**b**) H-field and (**c**) surface current distribution of the designed MUC.

Maxwell's equations[41,42], where the electric ($\vec{D}$) and magnetic field induction ($\vec{B}$) can be described by Eqs. 4 and 5. The ε_o and μ_o represent the permittivity and permeability of free space ε_r, and μ_r represents relative permittivity and permeability.

$$\vec{D} = \varepsilon\vec{E} = \varepsilon_o\varepsilon_r\vec{E} \tag{4}$$

$$\vec{B} = \mu\vec{H} = \mu_o\mu_r\vec{H} \tag{5}$$

Figure 4 shows the E-field allocations of the intended MUC for 24 GHz, 28 GHz, 30 GHz, and 37 GHz frequencies, which shows the high E-field density at the left and right edges of the MUC. Also, the field intensity proportionally increases with frequency. This high E-field medium aggregates the incident EM wave to the propagation direction. The low magnetic field distribution of the designed MUC is presented in Fig. 4. The magnetic field intensity of the upper side of the metamaterial increases with the frequency, and the lower side of the MUC proportionally decreases. The surface current allocation of the MUC is presented in Fig. 4, where anti-parallel current flow appeared at the splits of the MUC. The surface current intensity gradually decreases with the increment of the frequency. This property makes EM wave aggregation capability higher at the upper-frequency region than at the lower frequency.

Broadband dipole antenna design and metamaterial incorporation

Single antenna design

The design configuration of the proposed broadband dipole antenna (BDA) is depicted in Fig. 5. The antennas were designed on Rogers RT5880 substrate material with a dielectric constant of 2.2, a loss tangent of 0.0009, and a substrate thickness of 0.254 mm. The low dielectric constant is chosen for its ability to reduce electrical power loss at the higher frequency application[43]. On the other hand, low substrate thickness would decrease the end-fire cross-polarisation[44]. The substrate feature improves the antenna results parameters at the higher frequency regions. The designed antenna is fed by a W4 = 0.71 mm feed line, which is a series with W3 = 0.5 mm and a 0.3 mm width inverted U-shaped structure. All gematrical sketches of the intended antenna are presented in Fig. 5, and the design's parameter values are listed in Table 1.

The return loss (S_{11}), efficiency, and gain plot of the designed antenna are presented in Fig. 6. This demonstrates the realized gain of the designed antenna between the range of 4.7 to 6 dBi at the resonant bandwidth (24.35–38.7 GHz). The maximum 6 dBi gain appeared at the 34 GHz frequency. Conversely, the efficiency shows around 95% at the resonant bandwidth. The intended antenna radiation pattern at 26 GHz and 28 GHz frequencies in the E-plane and H-plane is presented in Fig. 7. The pattern shows good directivity of the designed BDA. The cross-polarisation is lower than 8 dB, and front to the back ratio of co-polarisation is more than 15 dB for the entire operating frequency. Figure 8 presents the designed antenna's electric (E) and magnetic (H) field distribution. The E-field intensity of the dipole arm is higher at 28 GHz frequency than at 26 GHz, which indicates the higher directivity and gain at 28 GHz frequency.

Figure 9 shows the bandwidth (S_{11}) plot of the different designs. In design one, the BDA does not show any resonance because of the incompetence of the feeding. The feeding on the dipole is completed in design two by making a slot line from the middle of the dipole to the inverted U shape. This design shows 5.54 GHz (− 10 dB) bandwidth from 30 to 35.54 GHz. The antenna's bandwidth is further enhanced in design 3 by making an elliptical slot at the center of the inverted U-shaped line, which increases the − 10 dB resonance bandwidth (10.8 GHz) from 28 to 38.8 GHz. Finally, a broadband 14.35 GHz (− 10 dB) bandwidth is achieved from 24.35 to 38.7 GHz frequency by declining the dipole arm by 40-degree.

Metamaterial incorporated antenna

The BDA's gain is increased significantly by incorporating the metamaterial structure into the propagation direction of the EM wave. Figure 10 shows the gradual incorporation of HRIM. The S_{11} of the different HIRM stages

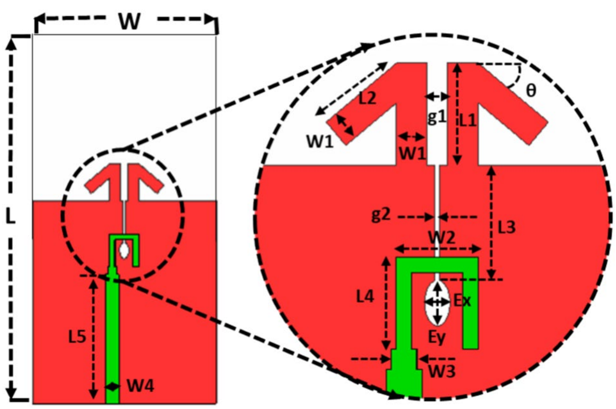

Fig. 5. Front view of a designed BDA with design parametric sketch.

Parameters	Value (mm)	Parameters	Value (mm)	Parameters	Value (mm)
W	10	W4	0.71	L5	7
L	18	L1	2	g1	0.4
W1	0.6	L2	1.8	g2	0.10
W2	1.6	L3	2.26	Ex	0.25
W3	0.5	L4	1.8	Ey	0.45

Table 1. Design parameters.

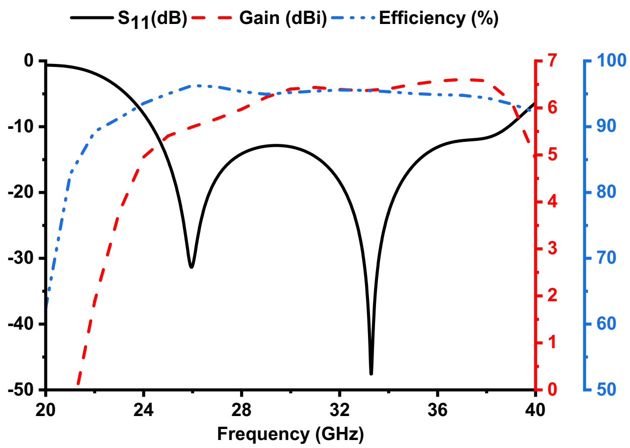

Fig. 6. Efficiency and gain plot of the designed BDA.

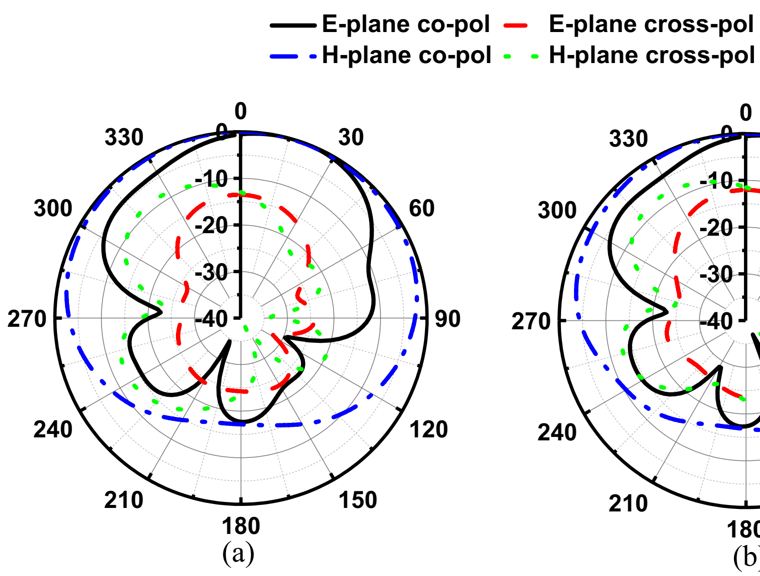

Fig. 7. simulated radiation pattern of the designed BDA.

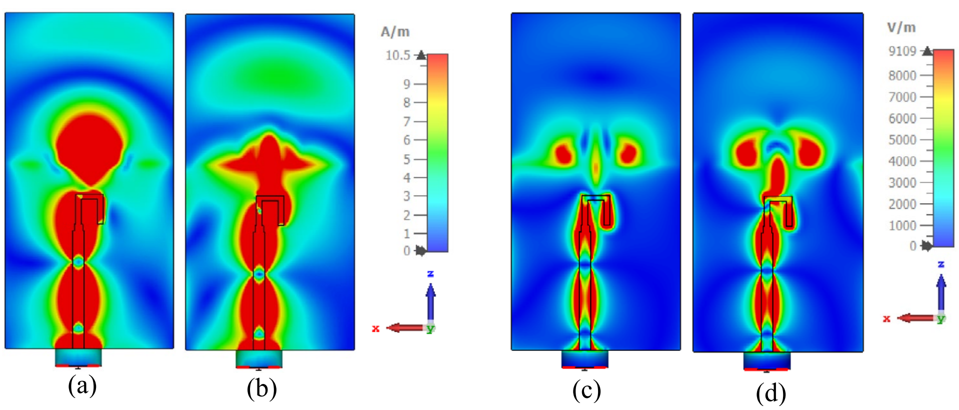

Fig. 8. Magnetic (H)-field at (**a**) 26 GHz, (**b**) 28 GHz and electric (E) field (**c**) 26 GHz, (**d**) 28 GHz of the designed BDA.

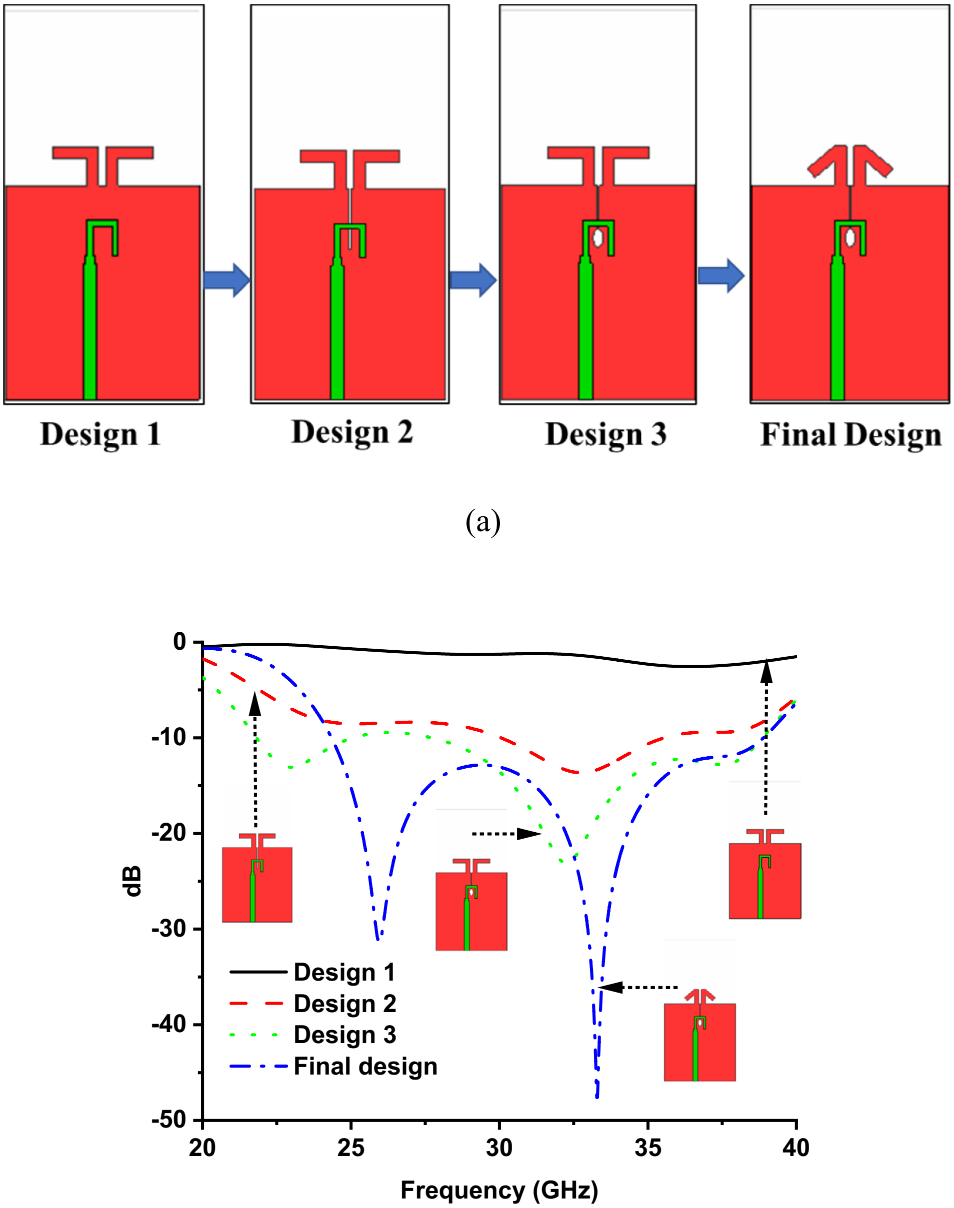

Fig. 9. (**a**) design evaluation of the BDA. (**b**) reflection coefficient (S_{11}) of the different steps of antenna designs.

is outlined in Fig. 11a, which shows a stable − 10 dB impedance bandwidth. The operational bandwidth of the final 5 × 6 HRIM appeared from 23 to 38 GHz frequency. The HRIM's effect on the BDA's gain is illustrated in Fig. 11b. The BDA's gain increases gradually with the increase of the HRIM unit cell series, and for the final 5 × 6 HRIM base antenna, the gain is achieved from 6 to 9.5 dBi. The highest gain of the antenna reached 9.5 dBi at 35 GHz resonant frequency. The equivalent circuit (EC) of the proposed HRIMDA is presented in Fig. 11c based on[45–47], where LC represent the feed line, $R_1L_1C_1$ and $R_2L_2C_2$ represent dipole antenna and $R_3L_3C_3$ represent HIRM. The EC is simulated by Advanced Design System (ADS) software, which agrees well with CST simulation shown in Fig. 11d. The EM wave aggregation property of the proposed HRIMDA can be understood from the antenna's electric, magnetic, and power flow. Figure 12 shows the proposed electric and magnetic fields at 26 and 28 GHz frequencies. The HRIM unit cell aggregates the EM wave in the direction of propagation. This EM wave aggregation engineering can be more clarified by the power flow of the HRIMDA, which is depicted in Fig. 13. The normal and HRIMDA power flow is presented to understand this behaviour. The circled region in Fig. 13 shows the power flow at the side edge of the antenna significantly reduced by the incorporation of HRIM on the antenna. The power flow significantly boosts the direction of the EM wave propagation.

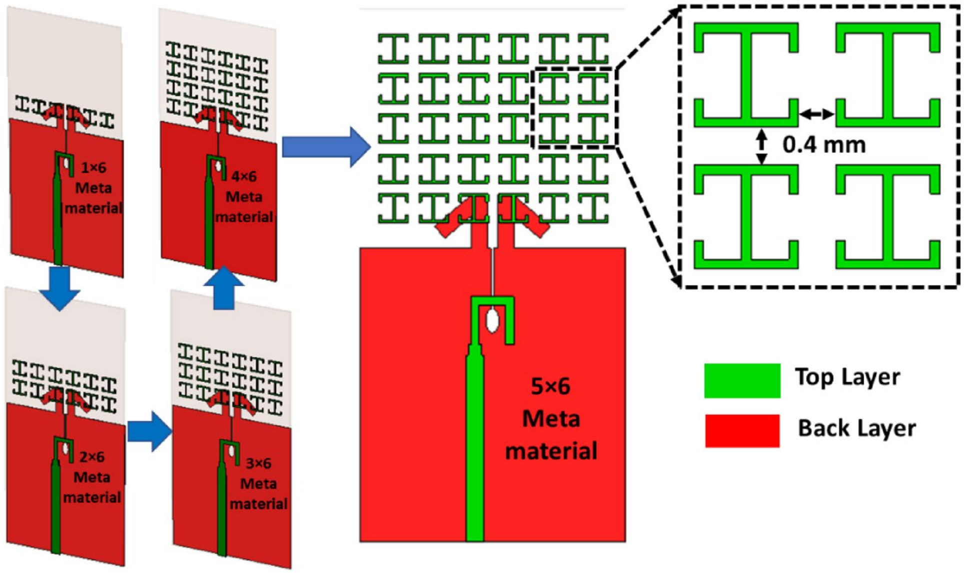

Fig. 10. Incorporation of the HRIM series on the BDA.

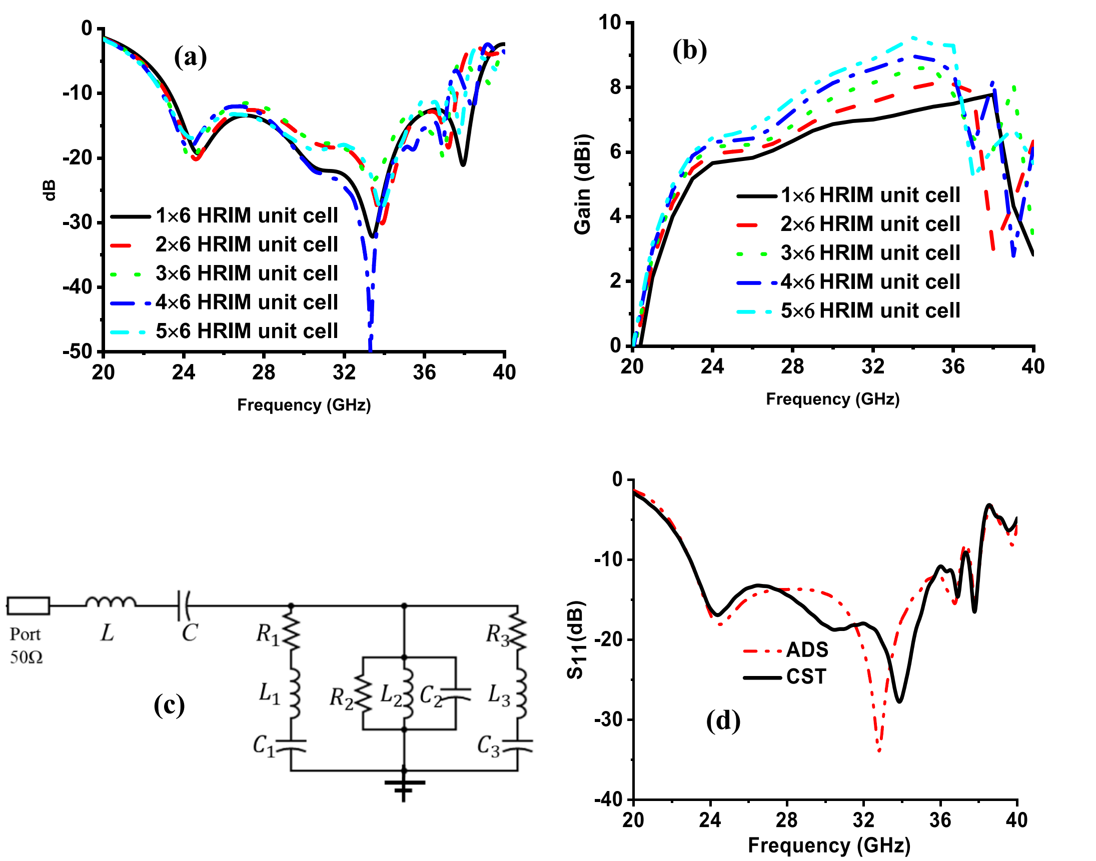

Fig. 11. (**a**) S_{11} and (**b**) gain plot of the intended HRIMDA at a different stage, (**c**) EC model ($L = 1.029$ nH $C = 0.0259$ pF, $R_1 = 3.493\ \Omega$, $L_1 = 1.814\ nH$, $C_1 = 0.00872\ pF$, $R_2 = 95.011\ \Omega$, $L_2 = 0.660\ nH$, $C_2 = 0.032\ pF$, $R_3 = 3.27\ \Omega$, $L_3 = 4.550\ nH$, $C_3 = 0.010\ pF$ and (**d**) S_{11} of ADS and CST simulation.

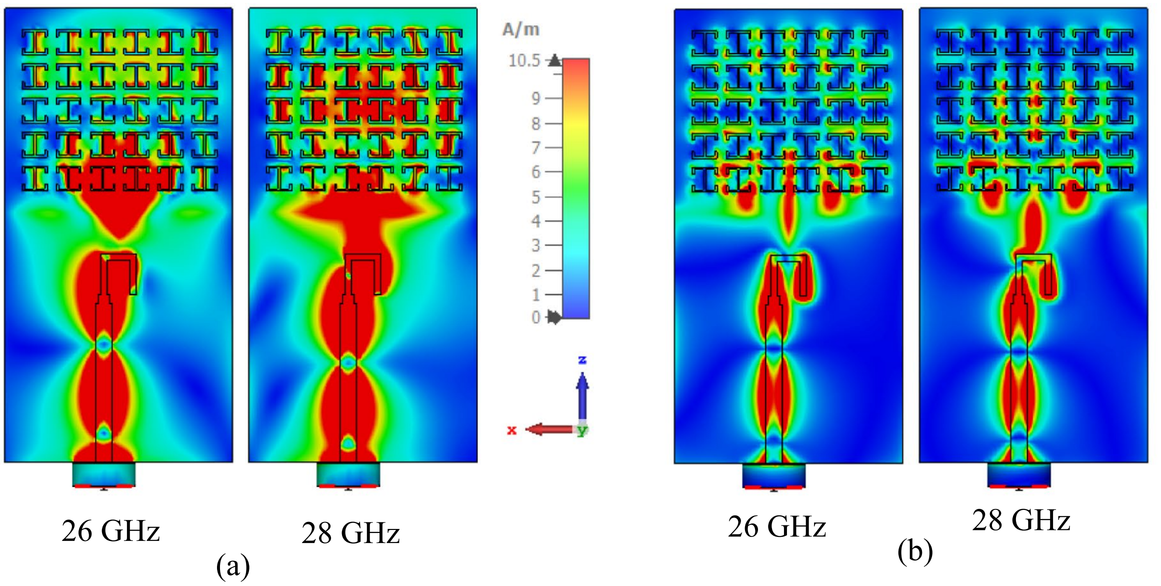

Fig. 12. (**a**) H-field distribution and (**b**) E-field distribution of the proposed HRIMDA.

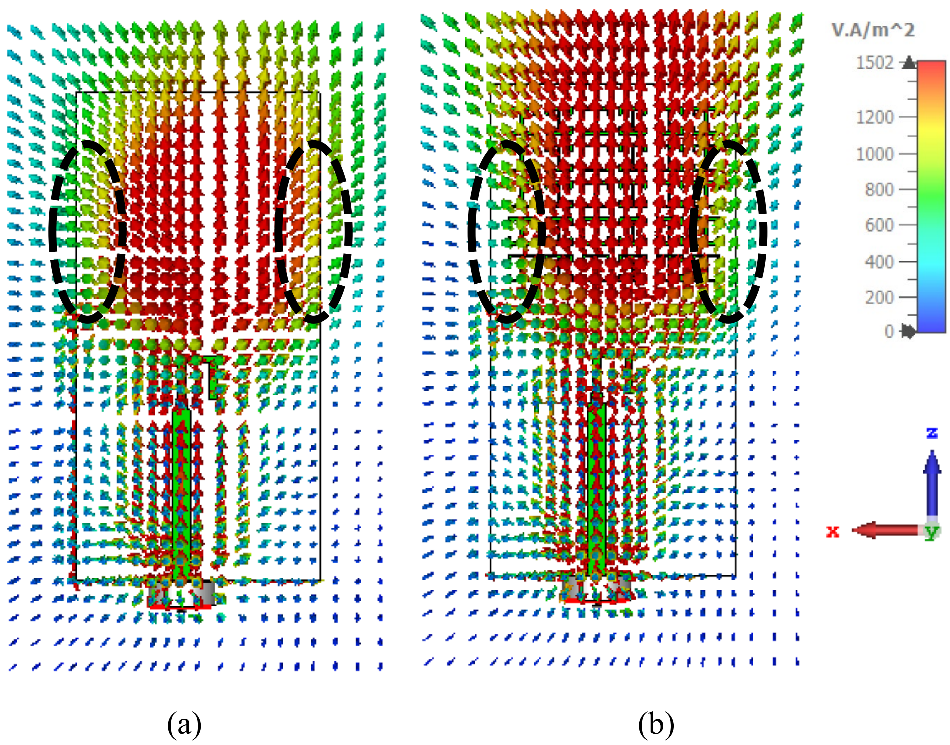

Fig. 13. Power flow at 28 GHz frequency (**a**) normal BDA and (**b**) proposed HRIMDA.

Fabrications and experimental results

To verify the intended HRIMDA's gain enhancement, two antennas (typical BDA and HRIMDA) were fabricated using 2.54 mm thin Rogers RT5880 ($\varepsilon_r = 2.2$) substrate material. The size of the antenna is 10×18 mm^2. Figure 14 shows the front and rear sides of the fabricated typical and HRIMDA. The vector network analyzer and far-field anechoic chamber measurement systems measured the fabricated antennas, as shown in Fig. 15. The simulated and measured S_{11} of the typical and HRIMDA is plotted in Fig. 16a, and the S_{11} of the fabricated antenna agrees well with the simulated one. The measured bandwidth of the HRIMDA is 23–38 GHz frequency. The measured gin of the normal and HRIMD is presented in Fig. 16b, which shows good agreement with the simulation results.

The simulated and measured E-plane and H-plane radiation patterns at 26 GHz and 28 GHz of the proposed HRIMDA are presented in Fig. 17. The measured radiation pattern agrees well with the simulated one. The

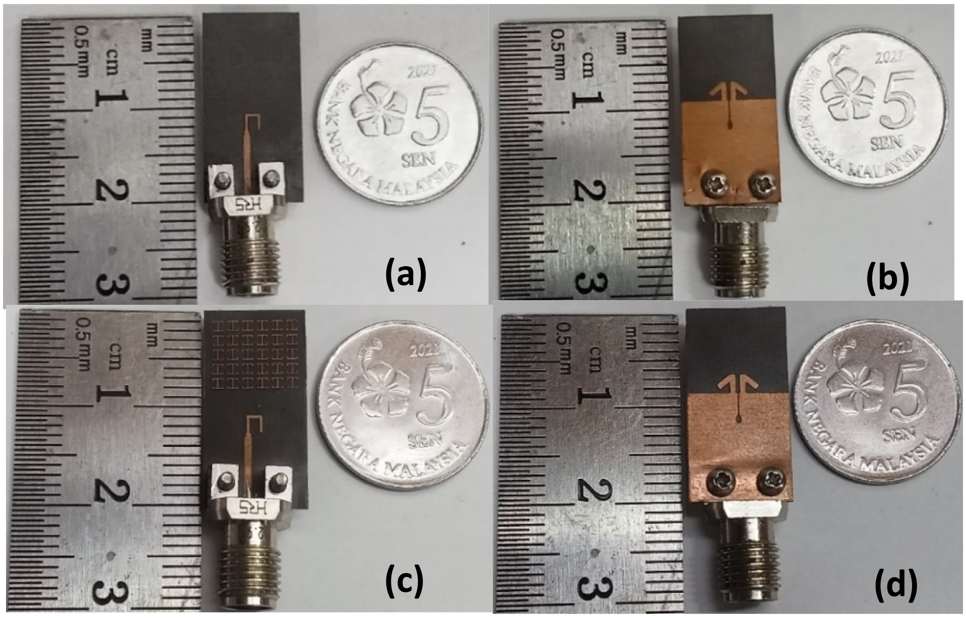

Fig. 14. Fabricated typical BDA (**a**) front view (**b**) rearview; and Fabricated HRIMDA (**c**) front view (**b**) rearview.

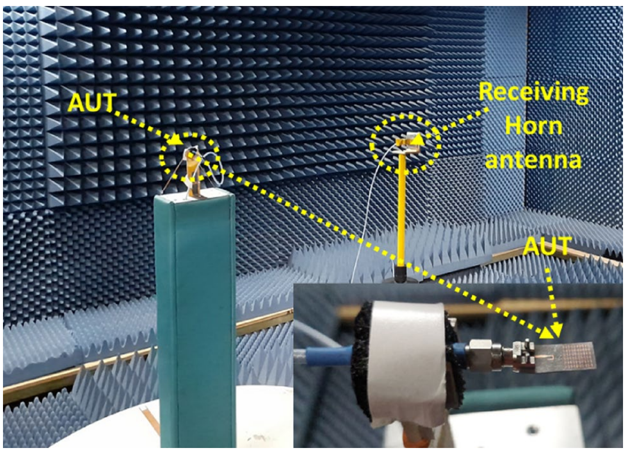

Fig. 15. Anechoic chamber measurement system.

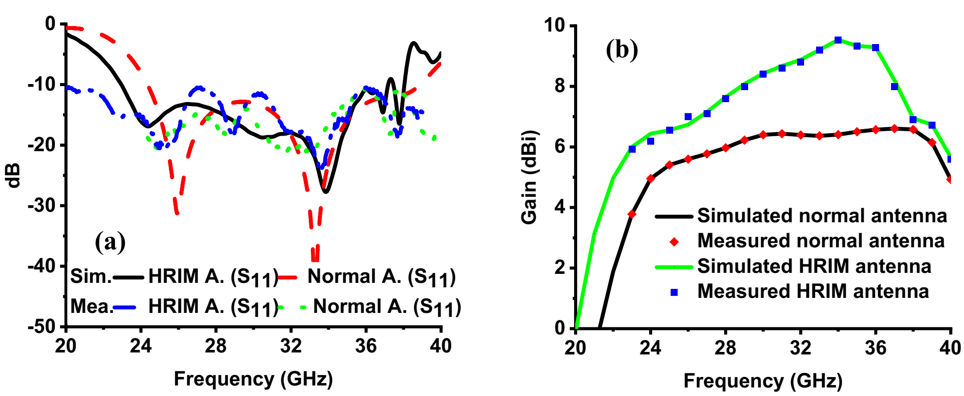

Fig. 16. (**a**) Simulated and measured S_{11}, and (**b**) Simulated and measured gain of the typical dipole and HRIMDA.

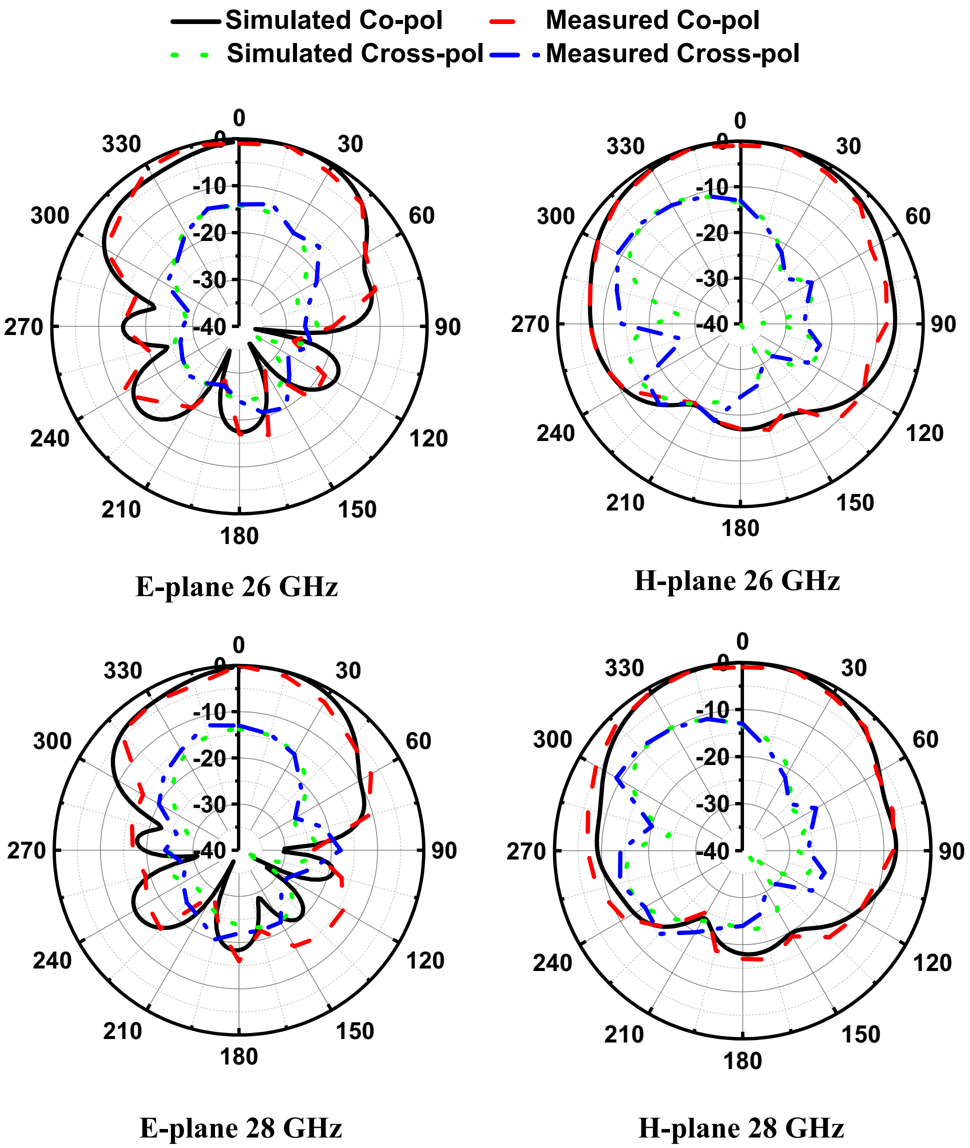

Fig. 17. Simulated and measured normalized radiation pattern of the intended HRIMDA.

cross-polarisation is less than 10 dB, and front to back ratio of the co-polarisation is less than 18 dB at the entire operating frequency, indicating the radiation beam's directivity. A detailed comparison of the proposed antenna with the existing broadband mm-wave antennas is presented in Table 2. The defective ground antenna is presented in[48,49], where wideband is achieved by defective ground technique but shows low antenna gain. Different planar-printed log-periodic dipole array (PLPDA) antenna types were presented in[38,39,50]. For broadband 5G mm-wave applications, the different types of MTM structures showed significant gains. A planar patch antenna[6], Shared aperture antenna[44], Bow-tie antenna[12] and Antipodal Vivaldi antenna[51] with meta-surface were presented for 5G applications, where the gain was improved significantly by utilizing different MTM structures. Multiple-layer microstrip antenna[22] and dual-layer two-element slotted patch antenna[52] are also presented, where MTM was placed on top of the antenna with an air gap. The MIMO parameters analyses were performed only in[6,22,52]. Finally, the proposed planar HRIMDA achieved a significant percentage bandwidth enhancement (BW %) compared to the other listed antenna. Also, HRIM enhances gain by 3.5 dBi, which is higher than the existing antennas. The investigation of the MIMO parameters analysis, compact antenna size, larger BW %, and higher gain prioritize the proposed antenna over the present antennas.

MMO configurations

Figure 18 shows a four-element MIMO antenna arrangement of the intended HRIMDA. The designed MIMO configuration is fabricated, and isolation of the two adjacent MIMO elements (antenna 2 and 3) is measured. The front and back views of the fabricated antenna are depicted in Fig. 19. Figure 20a shows the S_{11} of the simulated and measured MIMO elements. The simulated and measured isolation of the MIMO elements is depicted in Fig. 20b and c, where the measurement results agree well with the simulated results.

Ref.	Size (mm³)	Antenna design	Technique and MTM Structure	Layer	Air gap	Operation BW (GHz)	BW %	Gain Enhance dBi	MIMO
48	8 × 8 × 0.79 (0.7λ_0 × 0.7 λ_0 × 0.07 λ_0)	Umbrella-shaped patch antenna	No MTM is used	1	–	27.5–28.25 36.5–39.25 57–64	23.6 18.4 12.1	–	No
49	16 × 16 × 0.79 (1.3.λ_0 × 1.3 λ_0 × 0.065 λ_0)	Defected ground antenna	No MTM is used	1	–	25–50	66.6	–	Yes
50	13 × 22 × 0.508 (1.12λ_0 × 1.89 λ_0 × 0.043 λ_0)	Landstorfer PLPDA	Semi-circular splits ring	1	No	25.7–40	43.5	1.9	No
39	15 × 22 × 0.508 (1.3λ_0 × 1.91 λ_0 × 0.044 λ_0)	Clamped mode PLPDA	Semi ring patch	1	No	26–40	42.4	1.6 dBi	No
38	10 × 17.5 × 0.508 (1.34λ_0 × 2.37 λ_0 × 0.07 λ_0)	PLPDA	Bow tie directors	1	No	40–50	22.2	0.73	No
6	12.4 × 12.4 × 0.5 (1.0λ_0 × 1.0 λ_0 × 0.041 λ_0)	Patch antenna	Square patch Meta-surface	1	No	24.5–31	23.5	4	Yes
22	10 × 10 × ≈5.12 (0.94λ_0 × 0.94λ_0 × 0.48 λ_0)	Microstrip antenna	Cross shape	4	Yes	28–34	19.3	N/A	Yes
44	31 × 31 × 2 (2.71λ_0 × 2.71λ_0 × 0.181 λ_0)	Shared aperture antenna	Splits ring resonators	1	No	27–30	10.5	1.6	No
12	30 × 30.5 × 0.508 (2.46λ_0 × 2.5λ_0 × 0.041 λ_0)	Bow-tie antenna	Meander and triple I shape	1	No	24.5–27.5	11.5	2.9	No
51	40 × 24 × 1.6 (3.3λ_0 × 1.99λ_0 × 0.13 λ_0)	Antipodal Vivaldi antenna	Inverted V shape	1	No	24.8–34.52	32.7	1.78	No
52	17 × 11.7 × ≈7.6 (1.39λ_0 × 0.96λ_0 × 0.62 λ_0)	Two-element slotted patch antenna	Splits ring resonators	2	Yes	24.5–26.5	7.8	2.2	Yes
Proposed	10 × 18 × 0.254 (0.77λ_0 × 1.38λ_0 × 0.0195 λ_0)	Dipole antenna	Inverted dual C shape	1	No	23–38	49.2	3.5	Yes

Table 2. Comparison with the existing broadband mm-wave antenna.

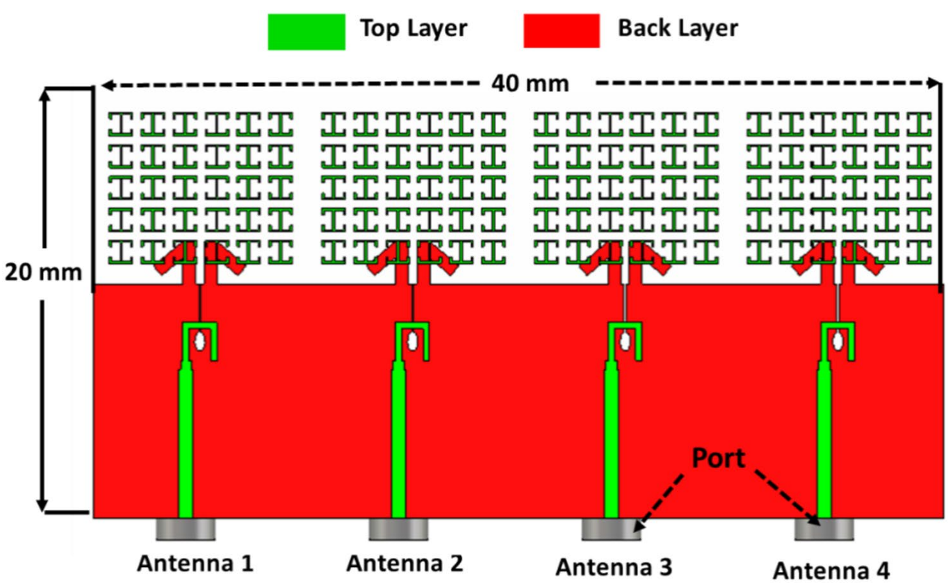

Fig. 18. Four-element MIMO antenna system.

The performance analysis of the designed MIMO antenna is done by investigating the envelop correlation coefficient (ECC) and diversity gain (DG). Equation 6 calculates the ECC value, which indicates the correlation of the MIMO antenna element. Equation 7 calculates the DG value, which indicates the impact of the antenna's radiated power diversity scheme.

$$\rho_{ec}(i,j) = \frac{\left|S_{ii} \times S_{ij} + S_{ji} \times S_{jj}\right|^2}{\left(1 - |S_{ii}|^2 - S_{ij}^2\right)\left(1 - \left|S_{ji}\right|^2 - S_{jj}^2\right)} \quad (6)$$

$$DG = 10 \times \sqrt{1 - \rho_{ec}} \quad (7)$$

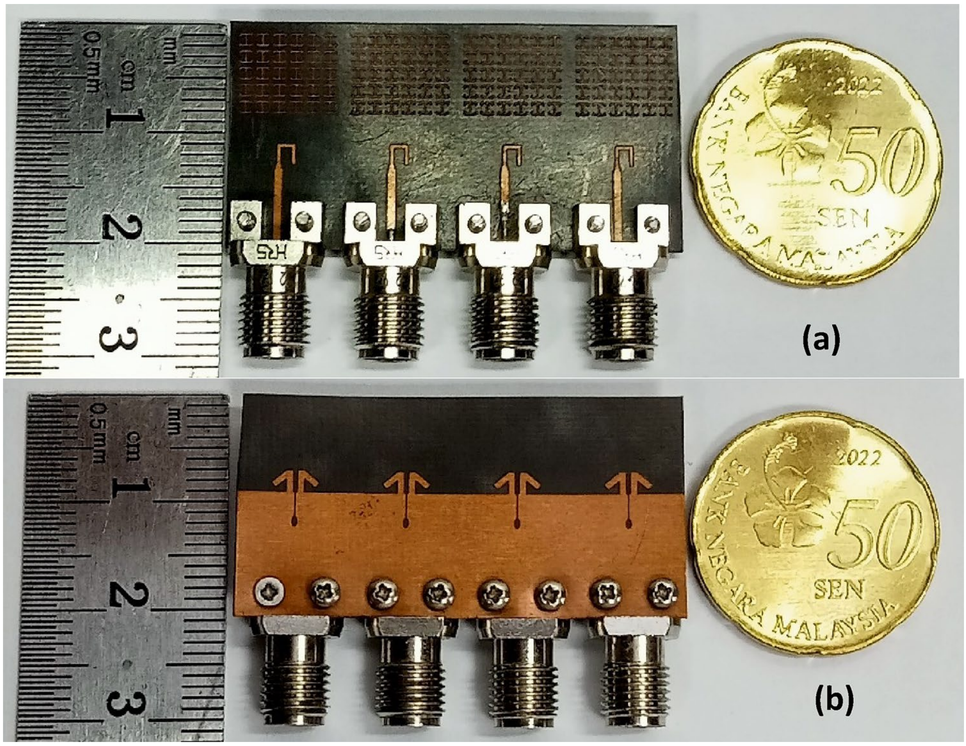

Fig. 19. Fabricated MIMO antenna (**a**) front view and (**b**) back view.

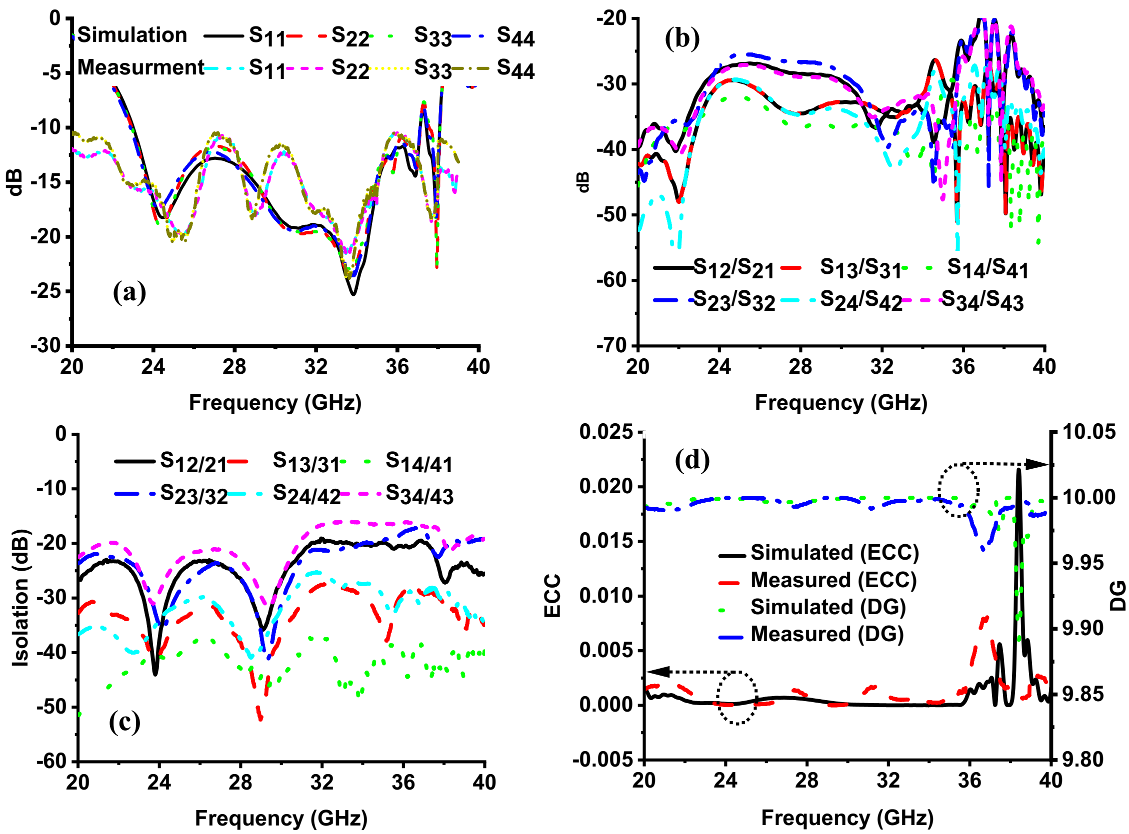

Fig. 20. Simulated and measured (**a**) S_{11} of the MIMO element, (**b**) Simulated isolation between the MIMO element, (**c**) Measured isolation between the MIMO element, and (**d**) MIMO parameters of two conjugate antennas (antenna 2 and 3).

Ref.	Elements	Frequency	Isolation	ECC	DG
[53]	4	25–39	< − 26	< 0.05	N/A
[54]	4	23.5–29.4	< − 22	< 0.004	N/A
[55]	4	27.5–40	< − 16	< 0.001	N/A
[56]	2	25–29,37–41	< − 24	< 0.001	> 9.9
[57]	4	27–30	< − 29	< 0.16	N/A
Proposed	4	23–38	< − 20	$< 1 \times 10^{-3}$	> 9.9

Table 3. Comparison of intended MIMO antenna and existing MIMO antenna.

In Eq. 6, S_{ii} and S_{jj} are the reflection coefficients; S_{ij} and S_{ji} ($i \neq j$) are the transmission coefficients of MIMO elements. The ECC value of the MIMO antenna should be less than 0.1, and a lower ECC value improves the MIMO performance. The simulated and measured ECC value of two conjugate antenna elements presented in Fig. 20d shows an ECC of less than $< 1 \times 10^{-3}$, which is the nearly ideal value. The simulated and measured DG value is achieved above 9.9, where the ideal value is 10. A comparison of the proposed four-element MIMO and existing MIMO configurations is presented in Table 3, where isolation, ECC, and DG value is compared. The intended MIMO antenna shows near the ideal value of both parameters compared to other existing MIMO antennas. This excellent feature makes the intended MIMO antenna a compatible candidate for mm-wave 5G applications.

Conclusion

An HRIMDA for mm-wave 5G applications is exhibited in this paper. A horizontal H-shape (HRIM) unit cell is modelled, and the unit cell's metamaterial property is utilized for gain enhancement. The designed antenna is fabricated and verified by measurement, where the single fabricated antenna has a small size of $0.77\ \lambda_0 \times 1.38\ \lambda_0 \times 0.0195\ \lambda_0$. The proposed HRIMDA shows − 10 dB (49.2 BW%) impedance bandwidth from 23 to 38 GHz frequency. The antenna gain notably improves by incorporating HRIM in the typical antenna and maximum enhancement by 3.5 dBi. The MIMO performance of the proposed HRIMDA is also investigated, which shows near the ideal value of ECC ($< 1 \times 10^{-3}$) and DG (> 9.9). Therefore, the proposed HRIM dipole antenna's excellent features make it an excellent candidate for upcoming advanced 5G applications, such as smart cities, autonomous vehicles, telemedicine, and enhanced mobile broadband. These applications require high data rates, low latency, and reliable connectivity, all of which are supported by the high gain and wide bandwidth of the HRIMDA. Additionally, the compact size and simple design of the antenna make it suitable for integration into various portable and fixed wireless devices. Finally, the HRIMDA represents a significant advancement in antenna technology for 5G mm-wave applications, combining high performance with practical design considerations. Its development paves the way for more efficient and reliable wireless communication systems, meeting the ever-growing demand for high-speed connectivity in our increasingly connected world.

Data availability

The data presented in this study are presented in this article.

Received: 12 July 2024; Accepted: 3 September 2024
Published online: 27 September 2024

References

1. FCC. America's 5G Future. FCC. https://www.fcc.gov/5G (Accessed 1 March, 2023).
2. Mallat, N. K., Ishtiaq, M., Ur Rehman, A., & Iqbal, A. Millimeter-wave in the face of 5G communication potential applications. *IETE J. Res.* 1–9 (2020).
3. Wang, S., Fu, X., Ruby, R. & Li, Z. Pilot spoofing detection for massive MIMO mm-wave communication systems with a cooperative relay. *Comput. Commun.* **202**, 33–41 (2023).
4. Baştürk, İ. Green communication for OFDMA cellular networks with multiple antennas. *Comput. Commun.* **168**, 93–101 (2021).
5. Hakim, M. L., Alam, T. & Islam, M. T. Polarization-insensitive and oblique incident angle stable miniaturized conformal FSS for 28/38 GHz mm-wave band 5G EMI shielding applications. *IEEE Antennas Wirel. Propag. Lett.* **22**(11), 2644–2648 (2023).
6. Hussain, N., Jeong, M.-J., Abbas, A. & Kim, N. Metasurface-based single-layer wideband circularly polarized MIMO antenna for 5G millimeter-wave systems. *IEEE Access* **8**, 130293–130304 (2020).
7. Hakim, M. L., Islam, M. T., & Alam, T. Incident angle stable broadband conformal mm-wave FSS for 5G (n257, n258, n260, and n261) band EMI shielding application. *IEEE Antennas Wire. Propagat. Lett.* (2023).
8. Sultan, K., Ikram, M. & Nguyen-Trong, N. A multiband multibeam antenna for sub-6 GHz and mm-wave 5G applications. *IEEE Antennas Wirel. Propag. Lett.* **21**(6), 1278–1282 (2022).
9. Soerbakti, Y. *et al.* Improvement of low-profile microstrip antenna performance by hexagonal-shaped SRR structure with DNG metamaterial characteristic as UWB application. *Alex. Eng. J.* **61**(6), 4241–4252 (2022).
10. Islam, M. S., Azam, S. K., Hossain, A. Z., Ibrahimy, M. I. & Motakabber, S. A low-profile flexible planar monopole antenna for biomedical applications. *Eng. Sci. Technol. Int. J.* **35**, 101112 (2022).
11. Hakim, M. L. *et al.* Interconnected square splits ring resonator based single negative metamaterial for 5G (N258, N257, N260 and N259) band sensor/EMI shielding/and antenna applications. *Alex. Eng. J.* **81**, 419–436 (2023).
12. Jiang, H., Si, L. M., Hu, W. & Lv, X. A symmetrical dual-beam bowtie antenna with gain enhancement using metamaterial for 5G MIMO applications. *IEEE Photonics J.* **11**(1), 1–9 (2019).
13. Hussain, M., Rafique, U., Dalal, P., Abbas, S. M., & Zhu, Y. A compact and wide band antenna for millimeter wave applications. In *2024 IEEE Wireless Antenna and Microwave Symposium (WAMS)*, IEEE, pp. 1–4 (2024).

14. Esmail, B. A., Koziel, S. & Szczepanski, S. Overview of planar antenna loading metamaterials for gain performance enhancement: The two decades of progress. *IEEE Access* **10**, 27381–27403 (2022).
15. C. Milias *et al.* Metamaterial-inspired antennas: A review of the state of the art and future design challenges. *IEEE Access* (2021).
16. Misran, N., Yusop, S. H., Islam, M. T. & Ismail, M. Y. Analysis of parameterization substrate thickness and permittivity for concentric split ring square reflectarray element. *Jurnal Kejuruteraan (J. Eng.)* **23**, 11–16 (2012).
17. Wu, W. J., & Wang, G. A modified AMC-based antenna sensor for contactless measurement of complex permittivity. Measurement, 112261 (2022).
18. Hussain, M. *et al.* Metamaterials and their application in the performance enhancement of reconfigurable antennas: A review. *Micromachines* **14**(2), 349 (2023).
19. Sonak, R., Ameen, M. & Chaudhary, R. K. High gain dual-band open-ended metamaterial antenna utilizing CRR with broadside radiation characteristics based on left-handed AMC and PEC. *Mater. Res. Express* **6**(5), 055811 (2019).
20. Jeong, M. J. *et al.* Millimeter-wave microstrip patch antenna using vertically coupled split ring metaplate for gain enhancement. *Microw. Opt. Technol. Lett.* **61**(10), 2360–2365 (2019).
21. Shaw, T., Bhattacharjee, D. & Mitra, D. Gain enhancement of slot antenna using zero-index metamaterial superstrate. *Int. J. RF Microwave Comput. Aided Eng.* **27**(4), e21078 (2017).
22. Akbari, M., Ghalyon, H. A., Farahani, M., Sebak, A.-R. & Denidni, T. A. Spatially decoupling of CP antennas based on FSS for 30-GHz MIMO systems. *IEEE Access* **5**, 6527–6537 (2017).
23. Khajeh-Khalili, F., Amin Honarvar, M., Dadgarpour, A. High-gain bow-tie antenna using array of two-sided planar metamaterial loading for H-band applications. *Int. J. RF Microwave Comput. Aided Eng.* **28**(7), e21476 (2018).
24. Yoon, N. N., Ha-Van, N. & Seo, C. High-gain and wideband aperture coupled feed patch antenna using four split ring resonators. *Microw. Opt. Technol. Lett.* **60**(8), 1997–2001 (2018).
25. Singha, R. & Vakula, D. Gain enhancement of the ultra-wideband tapered slot antenna using broadband gradient refractive index metamaterial. *Int. J. RF Microwave Comput. Aided Eng.* **28**(2), e21191 (2018).
26. Ullah, H. & Tahir, F. A. A high gain and wideband narrow-beam antenna for 5G millimeter-wave applications. *IEEE Access* **8**, 29430–29434 (2020).
27. Pant, M., & Malviya, L. Design, developments, and applications of 5G antennas: A review. *Int. J. Microwave Wire. Technol.* 1–27, (2022).
28. Nikam, P. B., Kumar, J., Sivanagaraju, V. & Baidya, A. Dual-band reconfigurable EBG loaded circular patch MIMO antenna using defected ground structure (DGS) and PIN diode integrated branch-lines (BLs). *Measurement* **195**, 111127 (2022).
29. Abbas, A. *et al.* Highly selective multiple-notched UWB-MIMO antenna with low correlation using an innovative parasitic decoupling structure. *Eng. Sci. Technol. Int. J.* **43**, 101440 (2023).
30. Reddy, G. N., Ravikumar, C., & Rajesh, A. Literature review and research direction towards channel estimation and hybrid precoding in mmWave massive MIMO communication systems. *J. Reliable Intell. Environ.* 1–20, (2022).
31. Bouknia, M. L. *et al.* Effect analysis of the general complex reciprocal gyro-bianisotropic metamaterial medium on the input impedance of a printed dipole antenna. *Alexandria Eng. J.* **61**(5), 3691–3696 (2022).
32. Zebiri, C. *et al.* Gyrotropic reciprocal bianisotropic metamaterial printed dipole antenna: Investigation of negative input impedance and mutual coupling. *Alexandria Eng. J.* **61**(12), 11677–11685 (2022).
33. Dwivedi, A. K., Sharma, A., Singh, A. K. & Singh, V. Metamaterial inspired dielectric resonator MIMO antenna for isolation enhancement and linear to circular polarization of waves. *Measurement* **182**, 109681 (2021).
34. CST Studio Suit. https://www.3ds.com/products-services/simulia/products/cst-studio-suite/ (Accessed 22 February, 2022).
35. Hakim, M. L., Alam, T., Almutairi, A. F., Mansor, M. F. & Islam, M. T. Polarization insensitivity characterization of dual-band perfect metamaterial absorber for K band sensing applications. *Sci. Rep.* **11**(1), 1–14 (2021).
36. Hakim, M. L. *et al.* Polarization insensitive symmetrical structured double negative (DNG) metamaterial absorber for Ku-band sensing applications. *Sci. Rep.* **12**(1), 1–18 (2022).
37. Chen, L., Lei, Z., Yang, R., Fan, J. & Shi, X. A broadband artificial material for gain enhancement of antipodal tapered slot antenna. *IEEE Trans. Antennas Propagat.* **63**(1), 395–400 (2014).
38. Chu, Q.-X., Li, X.-R. & Ye, M. High-gain printed log-periodic dipole array antenna with parasitic cell for 5G communication. *IEEE Trans. Antennas Propagat.* **65**(12), 6338–6344 (2017).
39. Zhai, G. *et al.* Gain-enhanced planar log-periodic dipole array antenna using nonresonant metamaterial. *IEEE Trans. Antennas Propagat.* **67**(9), 6193–6198 (2019).
40. Sun, Y., Du, Z., Du, J., Liu, Y. & Basit, M. A. Enhanced gain and broadband of endfire antenna by using I-shaped resonator structures. *Int. J. RF Microwave Comput. Aided Eng.* **28**(7), e21519 (2018).
41. Bait-Suwailam, M. M. Electromagnetic field interaction with metamaterials. *Electromagnet. Fields Waves,* 1–19 (2019).
42. Hakim, M. L. *et al.* Wide-oblique-incident-angle stable polarization-insensitive ultra-wideband metamaterial perfect absorber for visible optical wavelength applications. *Materials* **15**(6), 2201 (2022).
43. Campo, E. 4—Electrical properties of polymeric materials. *Select. Polym. Mater*. 141–173, (2008).
44. Sadananda, K. G., Abegaonkar, M. P. & Koul, S. K. Gain equalized shared-aperture antenna using dual-polarized ZIM for mmWave 5G base stations. *IEEE Antennas Wire. Propagat. Lett.* **18**(6), 1100–1104 (2019).
45. Khaleel, S. A., Hamad, E. K., Parchin, N. O. & Saleh, M. B. Programmable beam-steering capabilities based on graphene plasmonic THz MIMO antenna via reconfigurable intelligent surfaces (RIS) for IoT applications. *Electronics* **12**(1), 164 (2022).
46. Hamdan, S., Hamad, E. K., Mohamed, H. A. & Khaleel, S. A. High-performance MTM inspired two-port MIMO antenna structure for 5G/IoT applications. *J. Electric. Eng.* **75**(3), 214–223 (2024).
47. Khaleel, S. A., Hamad, E. K., Parchin, N. O. & Saleh, M. B. MTM-inspired graphene-based THz MIMO antenna configurations using characteristic mode analysis for 6G/IoT applications. *Electronics* **11**(14), 2152 (2022).
48. Hussain, M. *et al.* Design and fabrication of a printed tri-band antenna for 5G applications operating across Ka-, and V-band spectrums. *Electronics* **10**(21), 2674 (2021).
49. Hussain, M. *et al.* Ultra-wideband mimo antenna realization for indoor Ka-band applications. In *2022 United States National Committee of URSI National Radio Science Meeting (USNC-URSI NRSM)*, IEEE, pp. 108–109 (2022).
50. Chen, Y. *et al.* Landstorfer printed log-periodic dipole array antenna with enhanced stable high gain for 5G communication. *IEEE Trans. Antennas Propagat.* **69**(12), 8407–8414 (2021).
51. Dixit, A. S. & Kumar, S. The enhanced gain and cost-effective antipodal Vivaldi antenna for 5G communication applications. *Microwave Opt. Technol. Lett.* **62**(6), 2365–2374 (2020).
52. Tariq, S., Naqvi, S. I., Hussain, N. & Amin, Y. A metasurface-based MIMO antenna for 5G millimeter-wave applications. *IEEE Access* **9**, 51805–51817 (2021).
53. Khan, M. A. *et al.* mm-Wave four-element MIMO antenna for future 5G systems. *Appl. Sci.* **12**(9), 4280 (2022).
54. Sehrai, D. A. *et al.* Metasurface-based wideband MIMO antenna for 5G millimeter-wave systems. *IEEE Access* **9**, 125348–125357 (2021).
55. Al Abbas, E., Ikram, M., Mobashsher, A. T. & Abbosh, A. MIMO antenna system for multi-band millimeter-wave 5G and wideband 4G mobile communications. *IEEE Access* **7**, 181916–181923 (2019).
56. Ali, W., Das, S., Medkour, H. & Lakrit, S. Planar dual-band 27/39 GHz millimeter-wave MIMO antenna for 5G applications. *Microsyst. Technol.* **27**(1), 283–292 (2021).

57. Kamal, M. M. *et al.* Infinity shell shaped MIMO antenna array for mm-wave 5G applications. *Electronics* **10**(2), 165 (2021).

Acknowledgements

The authors would like to acknowledge the Universiti Kebangsaan Malaysia research grant Dana Impak Perdana 2.0 (DIP 2.0) through the grant number: DIP-2023-021. Also, the authors extend their appreciation to Taif University, Saudi Arabia, for supporting this work through project number (TU-DSPP-2024-11).

Author contributions

M.L.H, M.T.I, and T.A. made substantial contributions to this research work regarding the conception, design, analysis, measurement, and writing of the manuscript. M.S.J.S, M.S.S, A.M.A, and M.S.I made substantial contributions to this research work regarding conception, analysis, and revising the manuscript. M.T.I. supervised the entire project and acquired the portion of the funding. All authors have read and agreed to the published version of the manuscript.

Funding

This research was funded by the Universiti Kebangsaan Malaysia research grant Dana Impak Perdana 2.0 (DIP 2.0) through the grant number: DIP-2023-021. Also, the research was funded by Taif University, Saudi Arabia, Project No. (TU-DSPP-2024-11).

Competing interests

The authors declare no competing interests.

Additional information

Correspondence and requests for materials should be addressed to M.T.I. or M.S.I.